

Article

Facile Synthesis of Tin Dioxide Nanoparticles for Photocatalytic Degradation of Congo Red Dye in Aqueous Solution

Chih Ming Ma ^{1,*}, Gui Bing Hong ² and Shang Chieh Lee ²

¹ Department of Cosmetic Application and Management, St. Mary's Junior College of Medicine, Nursing and Management, No. 100, Lane 265, San-Shing Rd., Sec. 2, San-Shing Shiang, YiLan County 266, Taiwan

² Department of Chemical Engineering and Biotechnology, National Taipei University of Technology, No. 1, Sec. 3, Zhongxiao E. Rd., Taipei City 106, Taiwan; lukehong@ntut.edu.tw (G.B.H.); jack123565@gmail.com (S.C.L.)

* Correspondence: cmma@smc.edu.tw; Tel.: +886-3-9897396

Received: 4 June 2020; Accepted: 15 July 2020; Published: 16 July 2020



Abstract: This research work reports an approach used to prepare a SnO₂ photocatalyst by precipitation and calcination pathways and describes an investigation of the effects of preparation parameters on SnO₂ yield. The SnO₂ photocatalyst was further used for the photocatalytic degradation of Congo red (CR) dye, and the removal efficiency was optimized using response surface methodology. The results indicate that the SnO₂ photocatalyst yield was the highest in 0.05 M of the precursor, stannous chloride and 28 wt % ammonia as the precipitant, pH 10, at 30 °C. The transmission electron microscopy results of the SnO₂ photocatalyst illustrate that the average particle size was mainly around 30–50 nm and had a solid spherical shape. The X-ray diffraction results reveal that the prepared sample had a highly crystalline SnO₂ rutile crystal structure. The prediction and experimental results of the Response surface methodology (RSM) indicate that, when the reaction time was 97 min, the operating temperature was 47 °C, the photocatalyst dosage was 751 mg/L, and the optimal degradation rate of the CR dye was 100%. After five consecutive photodegradation reactions, the degradation rate remained at 100%. The results demonstrated that the SnO₂ photocatalyst prepared in this study possesses excellent reusability.

Keywords: Congo red; dye; SnO₂; photocatalyst; precipitation method

1. Introduction

As the demand for dyed products has increased, the discharge of dye wastewater has increased proportionally. Globally, dye wastewater released into the environment has become one of the primary sources of serious pollution [1]. Its release is not only a problem due to the color of the wastewater but also because several of its intermediate products are toxic. Congo red (CR) mainly exists in wastewater discharged from the textile, papermaking, printing, and leather industries [2]. CR is a type of azo dye derived from benzidine. Due to its complex chemical structure and high solubility in aqueous solutions, once discharged into the natural environment, CR is persistent and has low biodegradability. The metabolic intermediate of CR is benzidine, which is a known carcinogen and may also cause some allergic reactions [3].

Environmental problems caused by wastewater affect the environment and human health. Numerous wastewater treatment technologies exist (e.g., coagulation, adsorption, ion exchange, and activated sludge [4–9]); however, they have several drawbacks and limitations—they are expensive, time-consuming, and release a considerable amount of secondary pollutants during treatment.

Semiconductor materials, used as photocatalysts, are an emerging technology in sewage treatment [10]. Compared with other treatment methods, the photocatalytic wastewater treatment process has several advantages, which includes higher efficient decomposition, nonselective degradation, conductivity in a normal environment, and relatively low equipment requirements [11–14]. Oxygen in the air is used in a reaction with natural light sources to degrade organic pollutants into small molecules until complete mineralization or inorganization into nontoxic CO₂ and H₂O occurs. Metal oxide photocatalysts have high chemical stability, recyclability, and high reactivity, and they can convert toxic organic substances into nontoxic inert substances [15–17].

Tin dioxide (SnO₂) has been widely used in industry (e.g., in gas sensors, high-energy-density rechargeable lithium batteries, solar storage devices, and electrocatalytic and photocatalytic catalysts [18–21]). The preparation of small spherical photocatalyst particles with high crystallinity is critical because such particles have high stability and large surface area in aqueous solutions [21–24]. The SnO₂ photocatalyst can be prepared using different techniques (e.g., microwave, hydrothermal, precipitation, sol-gel, electrodeposition, and chemical vapor deposition [25–28]). However, most of the methods have some disadvantages, such as expensive instruments and complex starting materials or experimental conditions. Among these methods, the precipitation method is an effective technique used for photocatalyst preparation. Its advantages include being environmentally friendly, simple, rapid, and inexpensive [29,30]. For example, Kim et al. reported that SnO₂ is not well absorbed by the human body and does not produce significant human health effects [31]. Chakraborty et al. reported the advantages (e.g., inexpensive, low temperature and pressure) of SnO₂ nanoparticle synthesized using the precipitation and utilization of SnO₂ nanoparticle for the photocatalytic degradation of 4-aminopyridine [32].

Wastewater treatment processes optimization is currently a hot research area. Response surface methodology (RSM) has been applied for analyzing the effects of operation conditions, optimizing processes and products, and identifying interrelationships between operating parameters [33,34]. Many studies used the RSM to optimize various wastewater treatments, such as adsorption [35], electro-chemical processes [36], Fenton, electro-Fenton processes [37], and photocatalytic processes [33]. The motivation of this study was to synthesize a SnO₂ photocatalyst using a simple and environmentally friendly preparation method and to use this photocatalyst in photocatalysis experiments to evaluate the degradation performance and optimization of photocatalytic processes using the RSM.

Al-Hamdi et al., (2017) pointed out that SnO₂ is an environmentally friendly photocatalyst and seems to be economically feasible and a highly promising material for water treatment in environmental engineering [38]. Over the last few years, many studies reported that the modification of the SnO₂ reduces the band gap energy [39–41]. However, the photocatalytic system optimization of SnO₂ has received less attention. The purpose of this work is to prepare a SnO₂ photocatalyst by the precipitation technique and calcination pathways and, using RSM for system optimization, to increase the efficiency of the removal of the contaminants by photocatalytic processes. This study was divided into two stages. In the first stage, a precipitation method was used to prepare SnO₂ as the photocatalyst material, and four single-factor variables (precursor concentration, precipitant type, precipitant concentration, and synthesis temperature) were used to identify operating conditions for the optimal SnO₂ yield. Scanning electron microscopy (SEM), energy-dispersive X-ray spectroscopy (EDX), transmission electron microscopy (TEM), X-ray diffraction (XRD), Brunauer–Emmett–Teller (BET), and ultraviolet–visible spectroscopy (UV–vis) were used to characterize the synthesized SnO₂ photocatalyst. This included property analysis of the photocatalyst's surface morphology and structure, crystallinity, specific surface area, pore structure, and band gap. SnO₂ is a stable n-type semiconductor with a wide band gap [38], which makes the SnO₂ difficult to be activated by visible light. This disadvantage leads to relatively low light utilization efficiency of SnO₂. In the second stage of this study, the photocatalytic degradation of SnO₂ was tested under different operating conditions (i.e., photocatalyst dosage, operating temperature, and illumination time) to enable the photocatalytic degradation of CR dye under ultraviolet light. First, a single-factor variation experiment

was conducted to evaluate the range of experimental parameters. Subsequently, the conditions of the optimal photocatalytic degradation efficiency were identified through the RSM experimental design, and factors affecting degradation efficiency were discussed. Therefore, this study could provide useful data for the development of SnO₂ photocatalyst in the future.

2. Results and Discussion

2.1. Operating Conditions for the Preparation of SnO₂

In the SnO₂ preparation processes, the precursor concentration, precipitant agent, and reaction temperature are considered the most important parameters that can affect the SnO₂ photocatalyst prepared using the precipitation method. In this work, stannous chloride was dissolved in water and then alkali (precipitant) was added to facilitate the following reaction [42,43]:



The calcination process is a dehydration reaction and the oxidation produces SnO₂ nanoparticles [44], where the SnO to SnO₂ reaction occurs at temperatures above approximately 400 °C [42,45], as follows:



Figure 1 depicts the correlation between different precursor concentrations and SnO₂ yield. The SnO₂ yield of the experiments using sodium hydroxide as the precipitant reached 92.95%, and the highest yield of the experiments using ammonia as the precipitant reached 97.58%. The SnO₂ yield increased as the precursor concentration increased, reaching equilibrium at 0.05 M. In addition, when the precursor concentration was found to be overly high, precipitation occurred without the addition of precipitant. This finding is consistent with those of previous studies [29,38]. The precipitate was white insoluble stannous–chloride-precipitated Sn(OH)Cl in water. Because the experimental condition of high-concentration precursors might have affected the stability of the precipitation process, a precursor concentration of 0.05 M was used as the experimental follow-up condition for the preparation of photocatalyst materials.

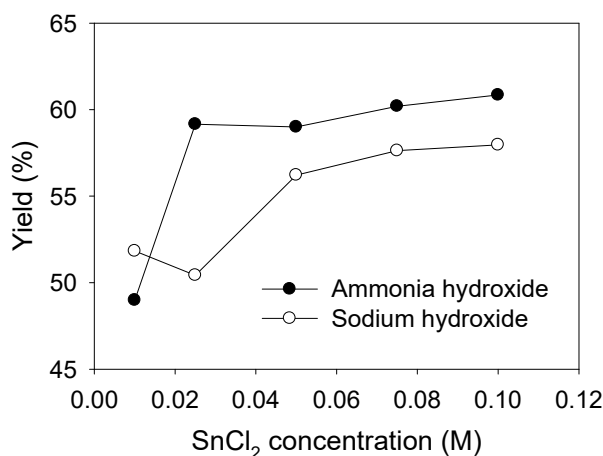


Figure 1. Effects of precursor concentration on the SnO₂ yield using ammonia hydroxide and sodium hydroxide as the precipitants.

Figure 2 depicts the correlation between the concentrations of different precipitants (sodium hydroxide and ammonia hydroxide) and yield. The trends indicated that the use of different precipitant

concentrations has slight effects on the yield. The yield of strong alkali sodium hydroxide at 1–4 M was in the range of $94\% \pm 3\%$, and the yield of weak alkali ammonia at 7–28 wt % was in the range of $98\% \pm 1\%$, indicating that the yield of ammonia was higher than that of sodium hydroxide. As the precipitant concentration of the ammonia increases, the light transmission in the samples are reduced, as shown in Figure 3a. The UV–vis full-wavelength spectrum indicated that the $\text{Sn}_6\text{O}_4(\text{OH})_4$ prepared using ammonia had a good stability of suspension. After the samples were left overnight, the ammonia sample was still suspended, and the sodium hydroxide sample was mostly precipitated. Therefore, 28 wt % ammonia was used as the follow-up experimental condition.

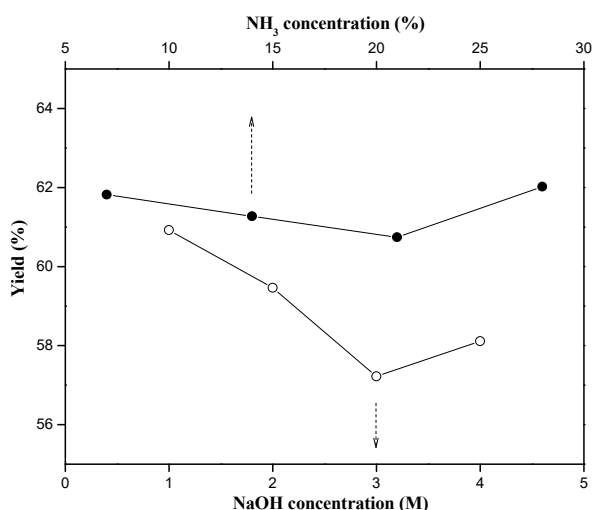


Figure 2. Effect of precipitant concentration on the SnO_2 yield.

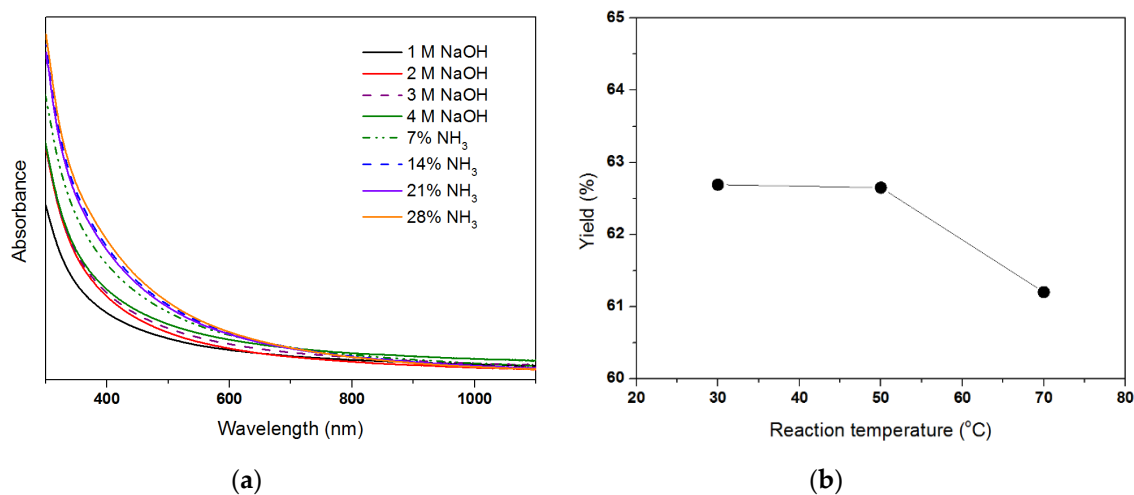


Figure 3. (a) UV–vis full-wavelength spectrum; (b) Effect of reaction temperature on the SnO_2 yield using ammonia hydroxide as the precipitant.

Finally, the precursor of 0.05 M stannous chloride and precipitant (28 wt % ammonia water) were used to indicate the effect of reaction temperature for the yield of products, as shown in Figure 3b. Our calculations indicated that the yields were all above 98%, and the range of yield change was not considerable. The reason for the slight decrease in yield at 70 °C could be that, as the temperature rose, the solubility of the precipitate increased, causing the yield to decrease slightly. Overall, the preparation process uses a single reactor and low-toxicity chemicals, and is inexpensive. It provides an economically viable and environmentally friendly method for synthesizing a SnO_2 photocatalyst.

2.2. Characterization of Photocatalyst

The morphology and elements of the photocatalysts were determined from SEM images and EDX analysis, respectively. Figure 4 depicts the SnO₂ samples synthesized using different precipitants; both were calcined at 600 °C and neither had an additional dispersant. This indicated that the samples with ammonia as the precipitant had smaller particles. EDX element analysis revealed that the presence of only Sn and O, and other impurities were not found. The appearance of other peaks (e.g., 2.2 keV) are due to borosilicate glass, gold sputter coating and carbon substrate tape used to paste the sample in the holder [39]. The morphology and the average particles size of SnO₂ samples synthesized by precipitation were revealed using TEM. Figure 5a shows the morphology of un-calcined Sn₆O₄(OH)₄, where un-calcined particles appear as irregularly-shaped polygons and an agglomeration phenomenon can be observed. Figure 5b shows that the SnO₂ particle profile after calcination was round and granular structures, but agglomeration still existed. SnO₂ particle size, as shown in Figure 5c, indicated a range of 20–80 nm and an average particle size of approximately 40 nm.

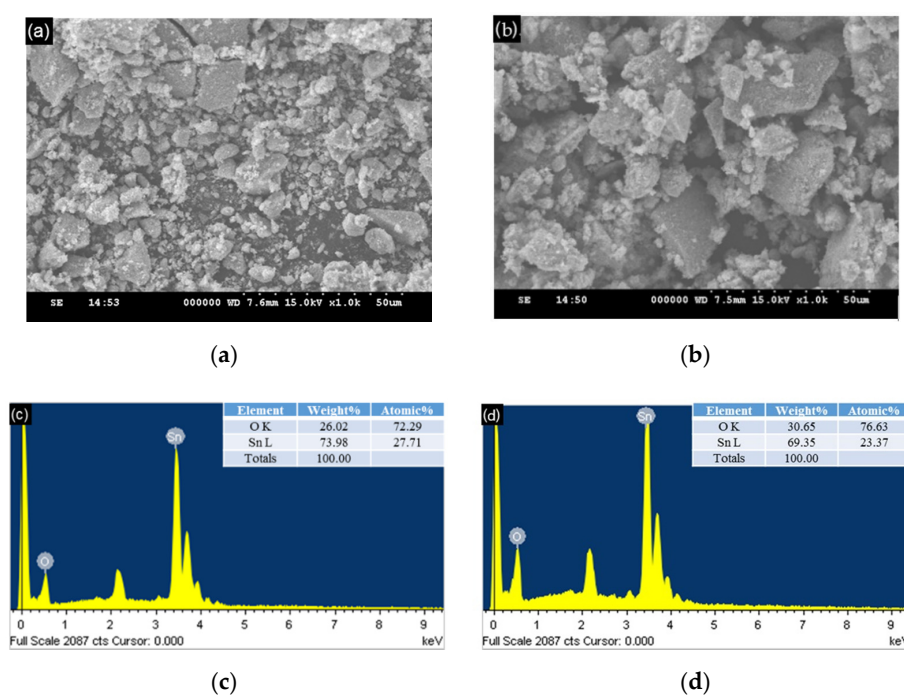


Figure 4. SEM images of photocatalyst with (a) sodium hydroxide and (b) ammonia as the precipitants; EDX analysis of photocatalyst with (c) sodium hydroxide and (d) ammonia as the precipitants.

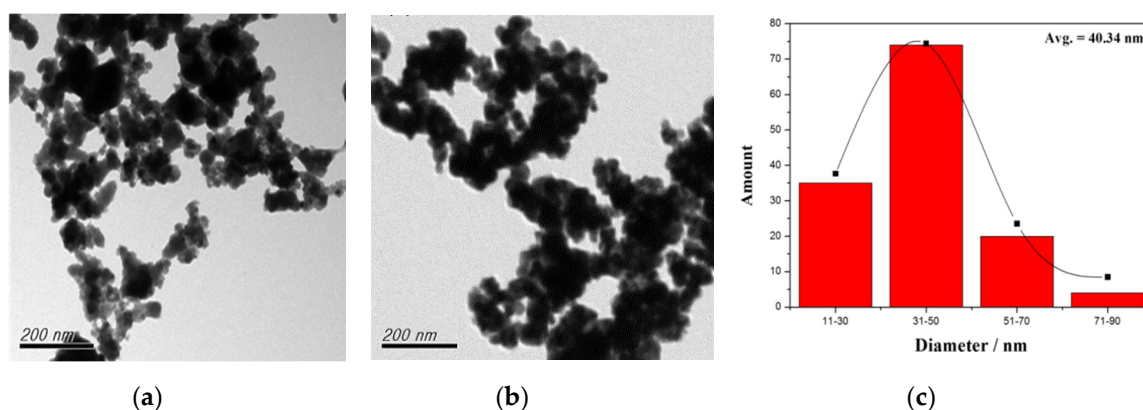


Figure 5. TEM images of (a) intact Sn₆O₄(OH)₄ before calcination; (b) SnO₂ after 600 °C calcination, and (c) particle size profiles of calcined SnO₂.

To understand the crystalline phase and structure, the synthesized SnO₂ samples were characterized by XRD. Figure 6a compares the XRD patterns before and after calcination. The sample before calcination was crystalline Sn₆O₄(OH)₄, the angle was 2θ, and the corresponding plane coordinates were 25.20° (112), 26.94° (211), 29.73° (202), 31.83° (212), 35.57° (310), 37.14° (311), 39.49° (004), 46.90° (313), 51.35° (420), 52.66° (332), 54.31° (314), 56.58° (413), and 59.19° (501). Analytical results were consistent with the comparison of JCPDS No. 01-084-2157, which confirmed that the sample was Sn₆O₄(OH)₄ crystal phase material. Besides, according to the XRD pattern of the standard card (JCPDS No. 00-041-1445) of SnO₂ sample calcined at 600 °C, it seemed to exhibit in the tetragonal rutile structure. No other impurity diffraction peaks were observed, which indicated that the purity of the prepared SnO₂ photocatalyst sample was high.

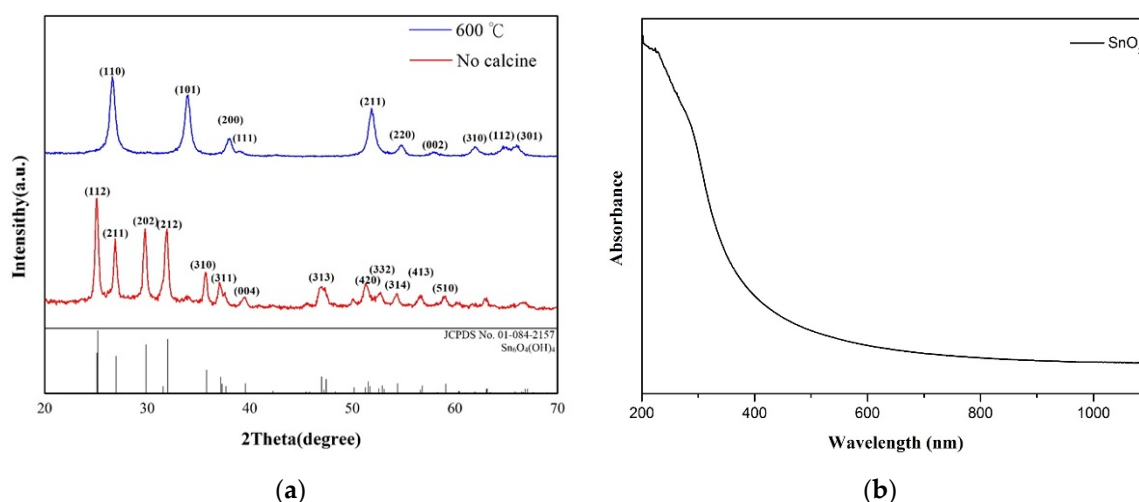


Figure 6. (a) The XRD spectra of un-calcined Sn₆O₄(OH)₄ and SnO₂ calcined at 600 °C (b) the UV–vis full-wavelength absorption spectrum of SnO₂.

Before the photocatalysis experiment, we used UV–vis to measure the full-wavelength absorbance of SnO₂ powder and to ensure that that the synthesized SnO₂ had photocatalytic activity. Figure 6a shows that the absorbance wavelength of the SnO₂ powder was in the ultraviolet wavelength range, and the band gap value of 3.575 eV was calculated using the Tauc plot method [46,47]. These values were similar to the band gap values found in earlier research studies [32,47]. As the literature [38] indicated, the band gap energy of SnO₂ of 3.1–3.9 eV should be activated by photons of a wavelength of 315–400 nm. That was why electrons from the valence band to the conduction band in SnO₂ synthesized could be excited by ultraviolet light (365 nm) irradiation, thereby producing the photocatalytic effect.

The specific surface area and pore size of the photocatalysts are also essential characteristics that can be used as indicators for the evaluation of the active sites and photocatalytic activity. The un-calcined samples and calcined samples at 600 and 700 °C were compared in terms of BET specific surface area, and the results are presented in Table 1. The BET-specific surface areas of each sample were 27.9671, 19.7177, and 14.3532 m²/g, respectively. The specific surface area of the un-calcined sample was the largest. As the calcination temperature rose, the specific surface area decreased, potentially because calcination at a higher temperature indicates a higher likelihood of SnO₂ melting and recrystallizing [48]. This would collapse the original pore defects and decrease the pore size distribution and total BET surface area.

Table 1. BET surface area of the $\text{Sn}_6\text{O}_4(\text{OH})_4$ and SnO_2 samples.

Materials	BET Surface Area (m^2/g)	Average Pore Volume (cm^3/g)	Pore Size (\AA)
Un-calcined ($\text{Sn}_6\text{O}_4(\text{OH})_4$)	27.967	0.043	611
600 °C	19.718	0.029	597
700 °C	14.353	0.018	514

2.3. Effect of the Operation Conditions on Photocatalytic Efficiency

To evaluate the photocatalytic efficiency of the prepared SnO_2 catalyst, the photocatalyst dosage, operating temperature, and initial concentrations were main factors considered as influencing the photocatalysis process. At a fixed operating temperature of 45 °C and a photocatalyst dosage of 500 mg/L, we conducted photodegradation of CR dyes with different initial concentrations (20, 30, and 40 ppm). The results indicated that the degradation rate of 20 ppm was faster at lower concentrations; for example, in a 45 min degradation reaction employed, degradation rates at 20, 30, and 40 ppm were 58.80%, 55.32%, and 47.19%, respectively, as shown in Figure 7. We can infer that the active site of the catalyst was blocked, which slowed the degradation. Alternatively, in the reaction with high dye concentration conditions, a considerable amount of light might have been absorbed by the dye molecules and decreased the penetration of light, thereby reducing the catalytic efficiency.

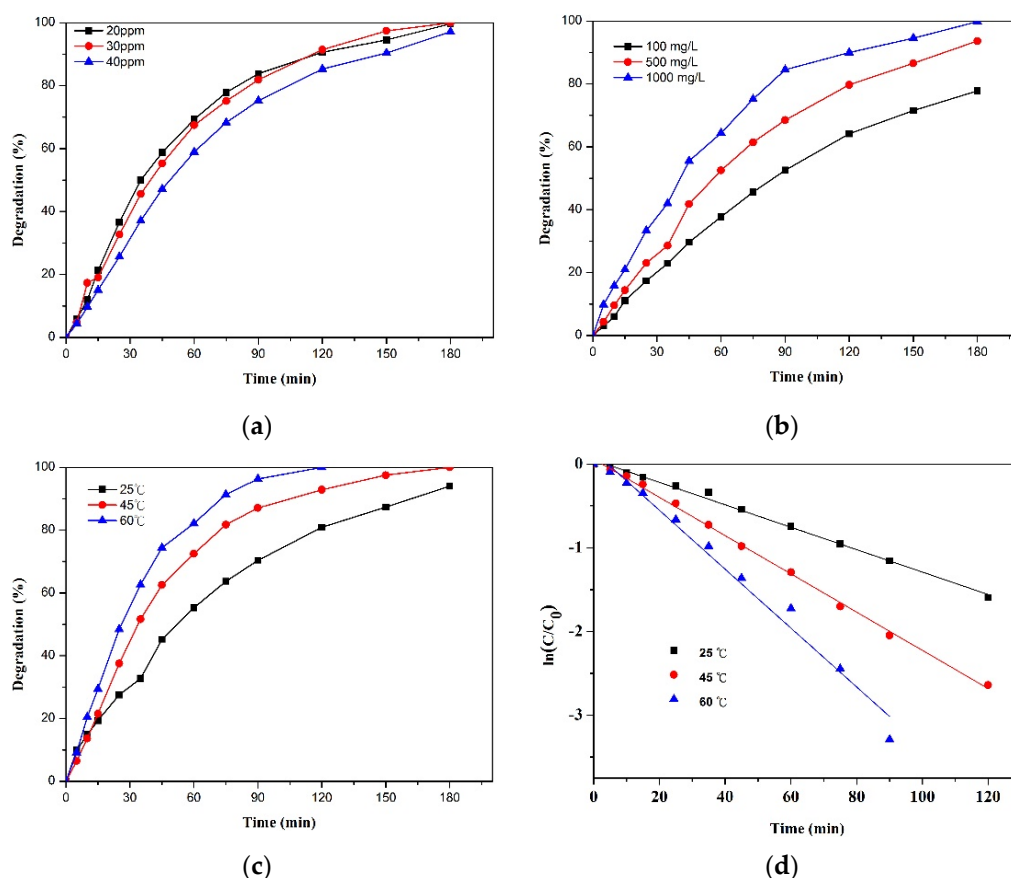


Figure 7. (a) Effect of different initial concentrations of CR on degradation efficiency; (b) Effect of different catalyst dosages on CR degradation efficiency; (c) Effect of different temperatures on CR degradation efficiency, and (d) the rate constants (k) of photodegradation.

The degradation of 20 ppm CR was performed at a fixed operating temperature of 25 °C. The degradation rate of CR increased with increasing catalyst dosage; for example, the rates for a 45 min degradation reaction at catalyst dosages of 100, 500, and 1000 mg/L were 29.64%, 41.80%, and 55.50%,

respectively, as shown in Figure 7b. The amount of SnO₂ catalyst is a crucial factor in the photocatalytic process due to its considerable influence on the rate of photocatalytic degradation. As the amount of catalyst increases, the active sites available for photocatalytic reactions increase; thus, the rate of dye removal increases. However, as the concentration of the catalyst increases and the particles aggregate, the specific surface area is likely to decrease, which would eventually lead to reduced photocatalytic activity [32]. An excessive amount of suspended catalyst particles would block the passage of ultraviolet light or sunlight and increase light scattering, thereby reducing the photocatalytic efficiency [12]. Nevertheless, under our experimental conditions, no reduction in efficiency was found.

Subsequently, 500 mg/L SnO₂ catalyst were used for the reaction condition in a 20 ppm CR solution. The effect of different degradation temperatures on the degradation rate was further tested. When the temperature was 25, 45, and 60 °C and the degradation time was 45 min, the degradation rates of CR were 45.18%, 62.53%, and 74.39%, respectively, as shown in Figure 7c. This indicated that, as the temperature increased, the photodegradation efficiency of the CR dye also increased. To understand the photocatalytic efficiency, we computed the rate constants using pseudo-first-order reaction kinetics, as shown in Figure 7d. The rate constants (k) of photodegradation at 25, 45, and 60 °C were 0.0134, 0.0228, and 0.0352 min⁻¹, respectively, and the R² (coefficient of determination) values were 0.9954, 0.9981, and 0.9832, respectively. The photodegradation of pollutants can be divided into two steps: adsorption and desorption on the catalyst and degradation on the catalyst's surface. First, increases in temperature seemed to be more favorable to dye adsorption and desorption on the photocatalyst [49]. Therefore, during the degradation of pollutants, the operating temperature slightly affects the ability of the photocatalyst to adsorb the dye. The size of the band gap changes with the temperature—as the temperature rises, the thermal energy could make the interatomic spacing increase, thereby weakening electrons bond and reducing the band gap [50,51]. The photogenerated electrons and electron holes generate more free radicals to react with pollutants to improve the degradation rate [52].

2.4. Optimization and Interactions of Photocatalysis Process

In this study, the BBD in the RSM was used to identify the optimal parameters for the SnO₂ photocatalytic degradation of CR. The control factors were the reaction time (15–150 min), operating temperature (30–60 °C), and catalyst dosage (100–1000 mg/L). In this experiment, the initial concentration of CR was fixed at 20 ppm, the volume of the CR solution was 500 mL, and the magnet was stirred at 400 rpm for photocatalytic degradation. Table 2 presents the experimental design table and experimental results. The experimental data were applied to evaluate linear, two-factor interaction, and quadratic models. The software recommended a quadratic model based on the analysis of the photocatalytic degradation model of CR. Following the model fitting, the second-order polynomial equation could be obtained, the calculation result of which was as follows:

$$\ln(\text{CR degradation rate}) = 4.41 + 0.72 \times A + 0.15 \times B + 0.19 \times C - 0.098 \times AB - 0.16 \times AC - 0.065 \times BC - 0.52 \times A^2 + 8.689 \times 10^{-3} \times B^2 - 0.088 \times C^2 \quad (5)$$

where A, B, and C are reaction times, temperature, and catalyst dosage, respectively. The predicted CR degradation rate was computed using Equation (5).

The quadratic model of the ANOVA results is summarized in Table 3. The determination coefficient (R²) of the empirical model was 0.9946, indicating that the model was suitable for analyzing the experiment results. The *p*-value of the model was <0.0001, which indicated that the effect of the second curvature on the response value was significant, which meant that the effect of the control factor on the response value was a curved relationship [34]. In Table 3, the *p*-values of A, B, C, A–B interaction, A–C interaction, A², and C² were all less than 0.05. This indicated that the contribution to the regression model was significant, whereas the contribution of the B–C interaction and B² to the regression model was non-significant [35]. The results of the lack-of-fit test were non-significant (*p*-value > 0.05), indicating that the quadratic model was suitable. The result of the analysis of the conformance of the CR degradation rate model's CV (coefficient of variation) was 1.64%. Predicted

R^2 (Pred. R^2) was 0.9427, suggesting that the model predicted the variance of the new experimental response value to be 94.27% [53,54]. Besides, Adjusted R^2 (Adj. R^2) was 0.9877 and the difference from Pred. R^2 value was less than 0.2, which expressed that the model was well fitted [36]. A higher Adequate Precision value also referred to the signal to noise ratio (SNR), which can indicate greater precision. An Adequate Precision value is more significant than four reasonable model prediction efficiencies [55]. Therefore, the results indicated that the model could effectively predict the degradation rate of CR.

Table 2. Box–Behnken design (BBD) matrix and Congo red (CR) dye degradation rate.

Run	Independent Variables			Responses
	X_1 : Time (min)	X_2 : Temperature ($^{\circ}$ C)	X_3 : Dosage (mg/L)	Dye Degradation Rate (%)
1	82.5 (0)	45 (0)	550 (0)	77.94
2	82.5 (0)	45 (0)	550 (0)	88.29
3	150 (1)	30 (−1)	550 (0)	93.97
4	82.5 (0)	30 (−1)	100 (−1)	50.35
5	15 (−1)	30 (−1)	550 (0)	19.97
6	82.5 (0)	45 (0)	550 (0)	79.31
7	82.5 (0)	60 (1)	100 (−1)	81.52
8	82.5 (0)	45 (0)	550 (0)	85.39
9	15 (−1)	45 (0)	100 (−1)	14.60
10	82.5 (0)	60 (1)	1000 (1)	100
11	82.5 (0)	30 (−1)	1000 (1)	80.03
12	150 (1)	45 (0)	1000 (1)	100.00
13	82.5 (0)	45 (0)	550 (0)	79.40
14	150 (1)	45 (0)	100 (−1)	90.71
15	150 (1)	60 (1)	550 (0)	100.00
16	15 (−1)	60 (1)	550 (0)	31.4
17	15 (−1)	45 (0)	1000 (1)	30.2

Table 3. Analysis of variance (ANOVA) of the empirical model.

Source	Sum of Squares	Degree of Freedom	Mean Square	F-Value	p -Value	
Model	5.91	9	0.66	143.84	<0.0001	significant
A	4.10	1	4.10	898.83	<0.0001	significant
B	0.19	1	0.19	40.84	0.0004	significant
C	0.28	1	0.28	61.13	0.0001	significant
A–B	0.038	1	0.038	8.42	0.0229	significant
A–C	0.100	1	0.100	21.81	0.0023	significant
B–C	0.017	1	0.017	3.68	0.0966	not significant
A ²	1.13	1	1.13	246.98	<0.0001	significant
B ²	3.179×10^{-4}	1	3.179×10^{-4}	0.070	0.7994	not significant
C ²	0.033	1	0.033	7.17	0.0316	significant
Residual	0.032	7	4.563×10^{-3}	-	-	-
Lack of Fit	0.020	3	6.702×10^{-3}	2.27	0.2229	not significant

Note: $R^2 = 0.9946$, Adj. $R^2 = 0.9877$, Pred. $R^2 = 0.9427$, CV = 1.64%, and adequate precision = 37.214.

The RSM can be used to analyze the response surface plot in a model to elucidate whether an interaction between various factors exists. The response surface plot depicts a three-dimensional (3D) plot and a contour map (2D) of the relationship between response factors and control factors. Figure 8a illustrates the relationship between reaction time and temperature. The 3D image shows a slightly distorted surface, which is a characteristic of an interaction effect [35]. The ANOVA suggested a p -value < 0.05, as shown in Table 3, which also meant that an interaction effect existed. However, the contour lines appeared to be straight, indicating that, although an interaction existed, the trend of the interaction relationship displayed on the graph is not evident because the effect of the reaction time

was overly broad. The dense distribution of lines on the x-axis indicates that the reaction time was the main factor affecting the level of degradation rate. Figure 8b also presents the relationships between reaction time and catalyst dosage. The contour line shows a micro-curved appearance and confirms the existence of an interaction. The ANOVA indicated a p -value < 0.05 , and thus an interaction existed. The line distribution density on the x-axis indicates that the reaction time still had a major effect on the level of degradation rate. Figure 8c presents the relationship between operating temperature and catalyst dosage. The 3D image was flat, which suggested that the operating temperature did not interact with the catalyst dosage. The ANOVA indicated a p -value > 0.05 , which meant that no interaction existed, and the density of the contour plot was evenly distributed among the two factors. Therefore, it was hard to determine the impact level between the operating temperature and catalyst dosage on the degradation rate from the response surface plot. However, the large F-value can be used to check statistical significance [33]. A higher F-value implied a more considerable influence on the CR degradation rate. Table 3 shows that the significant effects on CR degradation rate were in the following order: reaction times $>$ catalyst dosage $>$ temperature.

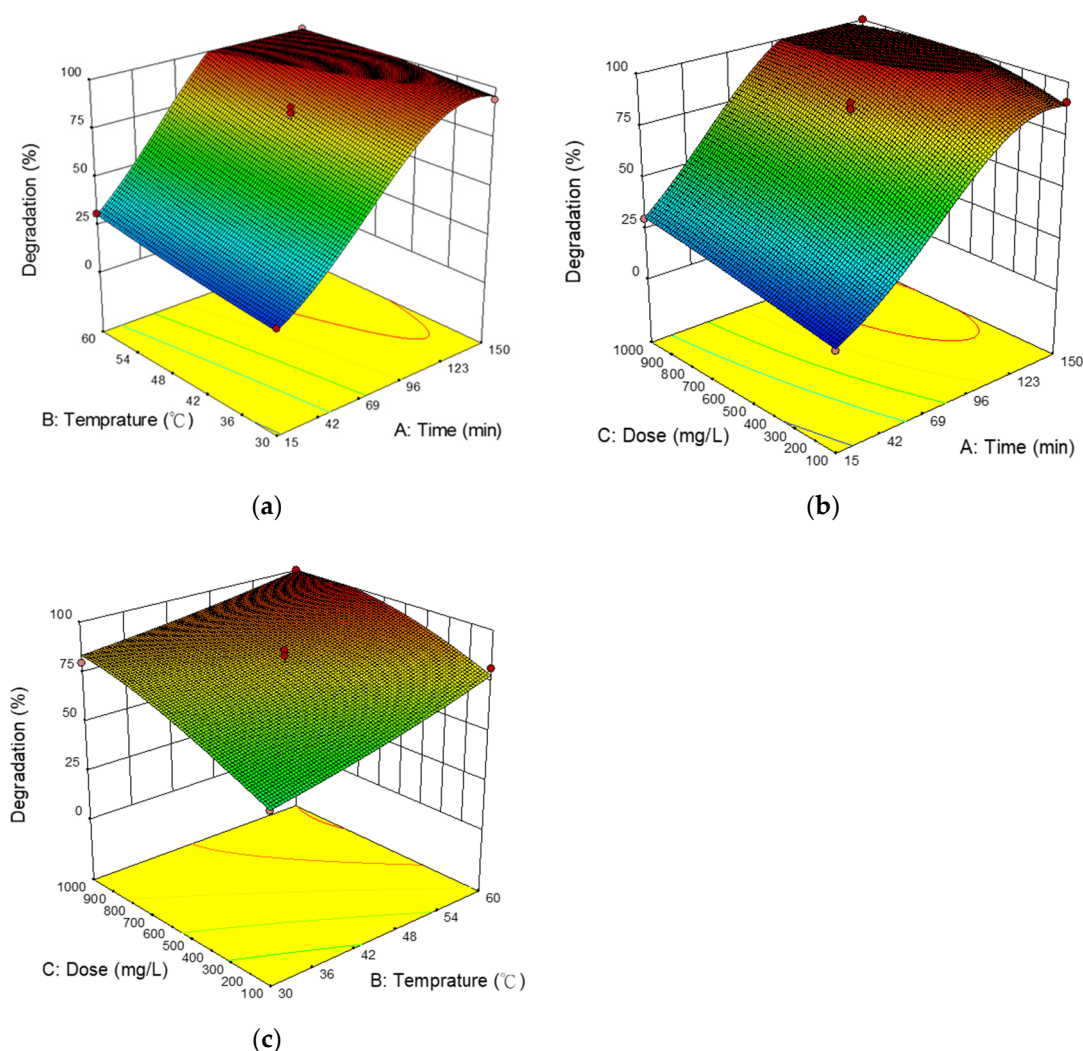


Figure 8. Response surface plot showing the effects of: (a) temperature and reaction time; (b) catalyst dosage and reaction time; (c) catalyst dosage and temperature.

The RSM model can be used for residual analysis (e.g., the model's normality, equal variance, and independence) to evaluate suitability [56]. If the residuals are normally distributed, the points depicting the residuals will resemble a straight line. The focus of the residual plot observation was

between 25% and 75%, indicating that both sides were not in an extreme state. Figure 9a presents a typical probability diagram of the residual of the CR degradation experiment. The distribution of each point of the experiment was closely aligned with the straight line and no outlier was observed. Accordingly, this experimental model did not violate the assumption of the normal behavior of the degradation rate of CR. We used residuals to analyze the scatter plots of the predicted values. If the graph had no shape or was it divergent or convergent, then the hypothesis that the number of residual variances is equal would be supported. The extra points in Figure 9b are randomly distributed and no flared funnel-shaped structure can be observed, and thus no divergence or convergence occurred. The even distribution of the residuals indicated that the predicted values were in a normal state. Therefore, the hypothesis that the variances of the CR degradation rate model are equal was supported.

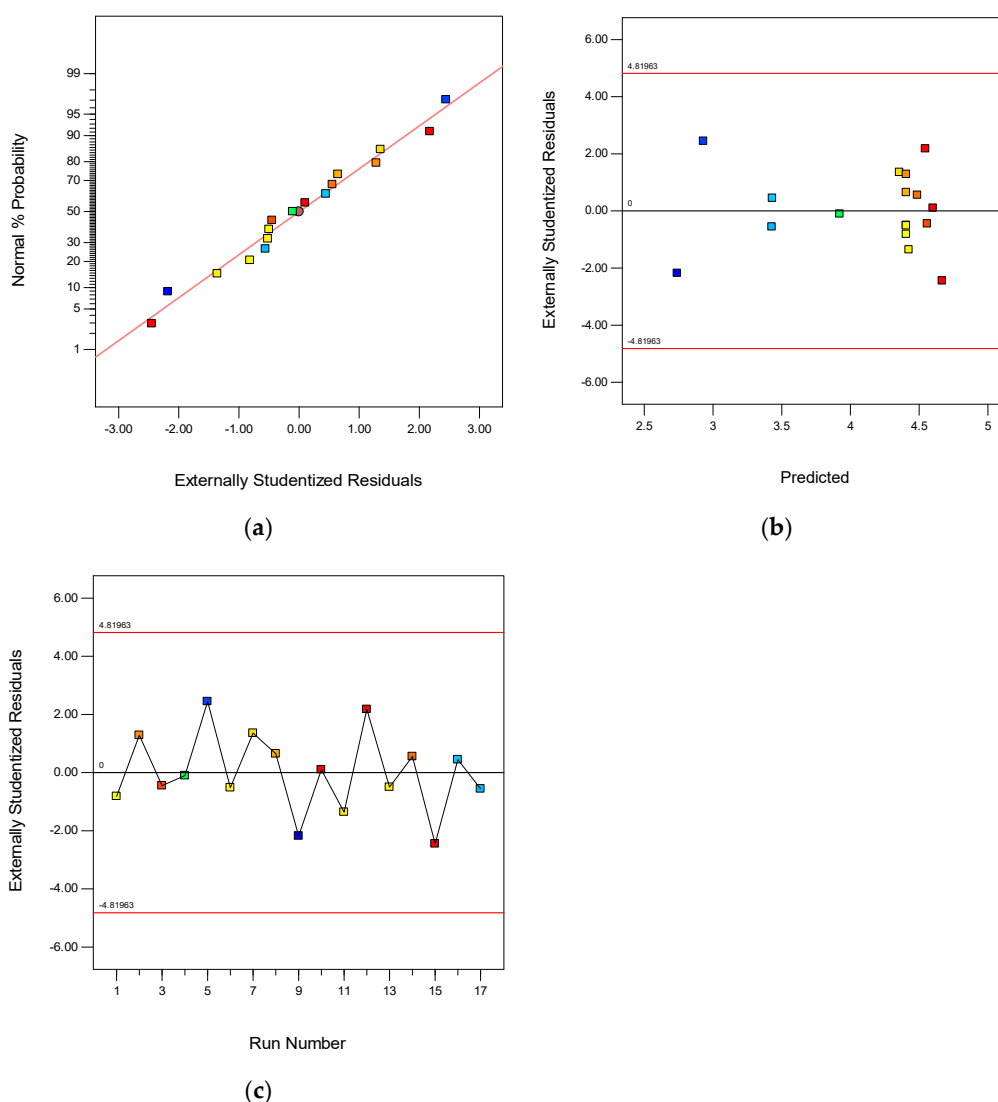


Figure 9. (a) Normal probability plot of residuals; (b) Residuals versus predicted response; (c) Residuals versus run for degradation of CR.

Residuals were plotted in chronological order of experimental data collected in this study. If a series of positive or negative residuals is observed, a strong correlation between the residuals exists, which would violate the assumption of residual independence. Figure 9c indicates that the residuals were randomly distributed and no series of positive or negative residuals existed. Therefore, the hypothesis of independence of the CR degradation rate model was supported [35].

To verify the feasibility of the RSM, we compared the predicted maximum degradation rate of CR and the experimental results under the optimum conditions. The predicted maximum for the degradation rate of CR using this model was 100% and the optimized photocatalytic conditions were: reaction time = 97 min; operating temperature = 47 °C; photocatalyst dosage = 751 mg/L. Under the optimized conditions, the experimental results suggested that the degradation rate of CR was 100%, which was consistent with the model prediction.

2.5. Photocatalyst Comparison and Reusability

As the literature revealed, dyes have been removed by photocatalysts for water treatment [31,57–62]. The photocatalytic degradation rate of SnO₂ prepared by the precipitation method, which compared with various photocatalysts used to remove dye from aqueous solutions was very promising, as shown in Table 4. The results suggest that using the RSM to optimize dye treatments could provide a better photocatalytic degradation rate than other studies. This optimization of photocatalytic processes using the RSM could be more favorably used in high concentration and short reaction time for dye removal.

Table 4. Comparison of dye photocatalytic degradation rate.

Catalyst	Prepared Method	Dye	Concentration (mg/L)	Reaction Time (min)	Degradation Rate (%)	Reference
SnO ₂	Liquid phase deposition	MB	10	180	51–82	[57]
SnO ₂	Hydrothermal	MB	10	120	90	[58]
SnO ₂	Co-precipitation	MB	25	60	60	[59]
SnO ₂	Biosynthesis	MB	80	180	88–91	[60]
SnO ₂	Precipitation	MB	10	180	80	[31]
ZnO	Microwave-hydrothermal	CR	160	180	43	[61]
ZnO	Green synthesis	CR	15	80	99	[62]
SnO ₂	Precipitation	CR	750	97	100	This study

For the industrial applications of photocatalysts, the recycling and reuse of the SnO₂ are essential components of the practical implementation of the water treatment process [18]. To investigate the reusability of the prepared SnO₂, we have selected the optimum conditions for the photocatalytic degradation of CR. At a CR concentration of 20 ppm, solution volume of 500 mL, operating temperature of 47 °C, catalyst dosage of 751 mg/L, and degradation reaction time of 97 min, five consecutive photodegradation experiments were conducted on the SnO₂ photocatalyst and the results are presented in Figure 10. As the number of cycles increased, the degradation rate remained at 100%, which indicates that the SnO₂ photocatalyst prepared in this research study has excellent reusability.

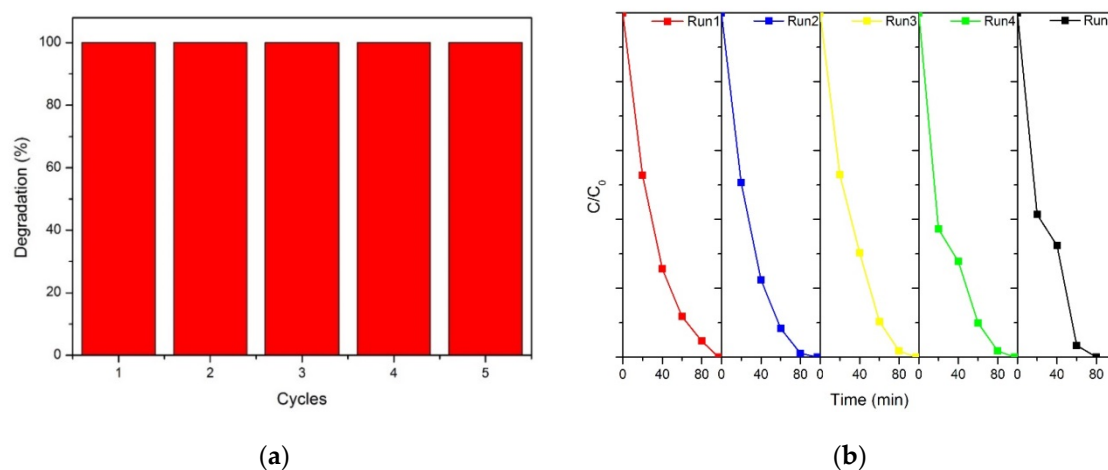


Figure 10. (a) Comparative performance of reused SnO₂ photocatalyst; (b) Time courses of five-cycle consecutive reused SnO₂ photocatalyst for dye degradation.

3. Materials and Method

3.1. Materials

Tin (II) chloride dehydrate (purity $\geq 99.8\%$), ammonia hydroxide (35%), sodium hydroxide (purity $\geq 97\%$), ethanol (purity $\geq 99.8\%$), and methanol (purity $\geq 99.9\%$) were purchased from Fisher Chemical (Pittsburgh, PA., USA). CR dye was supplied by Acros Organics (Geel, Belgium). All chemicals were analytical grade and used as received.

3.2. Preparation of SnO₂ by Precipitation

First, stannous chloride was placed in a 500 mL glass beaker to which 400 mL of deionized (DI) water was added and the solution was stirred with a magnetic stirrer (300 rpm). Synthesis was conducted at a rate of 1 mL of alkali (precipitant) added every 15 s until the pH reached 10. Subsequently, the solution was centrifuged in a 50 mL centrifuge tube to remove the supernatant, obtaining a white precipitate. After the precipitate was washed several times with 20 mL DI water, it was placed in an oven and dried at 50 °C for 24 h. The dried sample was ground into powder, the weight of which was recorded, and it was then placed in a glass sample bottle and stored in a dry box. Finally, the total amount of powder was placed in a crucible that was placed in a furnace for calcination at 600–700 °C for 2 h to obtain the SnO₂ photocatalyst.

The SnO₂ photocatalyst (final product after calcination) yield was calculated according to the following equation and used in the ensuing preparation experiments of SnO₂:

$$\text{SnO}_2 \text{ photocatalyst yield} = \frac{\text{number of SnO}_2 \text{ moles}}{\text{number of stannous chloride moles}} \times 100\% \quad (6)$$

3.3. SnO₂ Photocatalyst Characterizations

The surface morphology of photocatalysts was observed by a SEM (S-3000H, Hitachi Science and Technology, Tokyo, Japan). The elements of the SnO₂ photocatalyst were identified by EDX (Emaxx-act, Horiba, Kyoto, Japan). The size and morphology of SnO₂ particles were determined by employing TEM (H-7100, Hitachi, Tokyo, Japan). The XRD (Empyrean, Malvern Panalytical, Malvern, UK) was equipped with CuK α source ($\lambda = 0.151418$ nm) to understand the crystal structure of the sample under the following conditions: 40 kV/40 mA and 2θ range of 20°–70°. The specific surface area and pore size of the SnO₂ photocatalyst were analyzed using a BET measurements analyzer (Gemini™ V Series 2380, Micromeritics, Norcross, GA, USA). A GENESYS 10 Series spectrophotometer from Thermo Scientific (Waltham, MA, USA) was used for the observation of the UV–vis absorption spectra and the assessment of the photocatalytic degradation of the CR dye. The experiments were carried out in quartz cuvettes with 1 mm thickness.

3.4. Photocatalytic Degradation of CR Dye

In this experiment, before photodegradation, the CR dye contaminant solution (500 mL) and the photocatalyst were thoroughly stirred before being well dispersed with ultrasound by the ultrasonic cleaner (DC150, Delta Ultrasonic, Taiwan) for 1 min to disperse the catalyst evenly in the solution. Subsequently, they were placed in a dark room to enable the photocatalyst to adsorb the dye. When the adsorption reached equilibrium, we turned on the light source for degradation, which was a 400 W high-pressure mercury lamp with a main band of 365 nm. Magnetic stirring was performed at 400 rpm to conduct a photodegradation test for pollutants. During the degradation process, we used a syringe to draw 3.5 mL of solution at each sampling point, centrifuged the solution twice in a centrifuge (6000 rpm, 5 min), and then performed UV–vis to detect the absorbance value of CR and measure the change in its concentration. The dye degradation rate was calculated according to the following equation and used in the ensuing photocatalytic experiments:

$$\text{degradation rate (\%)} = \frac{C_0 - C}{C_0} \times 100\% \quad (7)$$

where C_0 and C are the dye concentration (mg/L) at initial time and at time t (min), respectively.

3.5. Process Variables and Experimental Design

For our experimental design, we used the software package Design Expert (Minneapolis, MN, USA) with the RSM as an extension method. The RSM combines mathematics and statistics and is the optimal tool for determining experimental design or operating parameters. First, we discussed the effect of single factors on the degradation rate of CR to determine the trend of each factor's degradation effect. To better understand the interaction of various factors, we employed the Box–Behnken design (BBD) which helps to explore the influence of the following three factors: X_1 : operating time (range 15–150 min), X_2 : operating temperature (range 30–60 °C), and X_3 : catalyst dosage (range 100–1000 mg/L). The BBD was composed of five central points and three-factor points, and its three levels were (−1, 0, +1). In total, 17 experiments were conducted. The experimental conditions and data are displayed in Table 2.

4. Conclusions

In the above research study, a SnO_2 photocatalyst was successfully prepared using the precipitation and calcination pathways method. The chemicals used in the synthesis process cause low harm to the environment and humans. Compared with other preparation methods, precipitation has various advantages, including speed, low cost, high purity, and higher yield. The results of the prepared process indicated that the photocatalyst yield of SnO_2 is affected by the precursor concentrations, synthesis temperature, and precipitant concentrations. Specifically, the effects of three single variables (initial concentration of pollutants, catalyst dosage, and operating temperature) on degradation efficiency were investigated for the CR dye. The degree of effects from high to low was as follows: operating temperature > catalyst dosage > initial concentration of pollutants. In the RSM, the interaction of the CR dye with three variables (reaction time, catalyst dosage, and operating temperature) was discussed. In the model simulation, only the interaction effects of B^2 (temperature) and BC (temperature, catalyst) was not noticeable and its model regression contribution was relatively small compared with the contribution of other factors. The prediction results of the model indicated that, when the degradation time was 97 min, the operating temperature was 47 °C, and the photocatalyst dosage was 751 mg/L, and the optimal degradation rate of the CR dye was 100%. We verified that the experimental values were the same as the predicted value of the model, which confirmed that the model was reliable. Finally, catalyst reusability was tested. After five consecutive photodegradation reactions, the degradation rate remained at the same level and the degradation efficiency was also 100%. This demonstrated that the SnO_2 photocatalyst prepared in this study has excellent reusability. The proposed precipitation method provides a simple and environmentally friendly preparation photocatalyst method. In the photocatalytic degradation of CR, through the RSM, these data could identify the optimal parameters for SnO_2 photocatalytic degradation and acknowledge the primary factors and two-factor interactions for water treatment applications.

Author Contributions: Conceptualization and methodology, G.B.H., S.C.L., and C.M.M.; investigation and formal analysis, S.C.L.; resources, G.B.H. and C.M.M.; data curation, S.C.L.; writing—original draft preparation, S.C.L. and C.M.M.; writing—review and editing, C.M.M. All authors have read and agreed to the published version of the manuscript.

Funding: This research was funded by Ministry of Science and Technology, ROC, grant number MOST105-2221-E-562-002-MY3.

Acknowledgments: The air pollution-controlled laboratory, National Ilan University, is thanked for access to experiment facilities.

Conflicts of Interest: The authors declare no conflict of interest. The funders had no role in the design of the study; the collection, analyses, or interpretation of data; in the writing of the manuscript, or in the decision to publish the results for this study.

References

1. Moreira, F.C.; Boaventura, R.A.R.; Brillas, E.; Vilar, V.J.P. Electrochemical advanced oxidation processes: A review on their application to synthetic and real wastewaters. *Appl. Catal. B* **2017**, *202*, 217–261. [[CrossRef](#)]
2. Han, R.; Ding, D.; Xu, Y.; Zou, W.; Wang, Y.; Li, Y.; Zou, L. Use of rice husk for the adsorption of congo red from aqueous solution in column mode. *Bioresour. Technol.* **2008**, *99*, 2938–2946. [[CrossRef](#)] [[PubMed](#)]
3. Lachheb, H.; Puzenat, E.; Houas, A.; Ksibi, M.; Elaloui, E.; Guillard, C.; Herrmann, J.M. Photocatalytic degradation of various types of dyes (Alizarin S, Crocein Orange G, Methyl Red, Congo Red, Methylene Blue) in water by UV-irradiated titania. *Appl. Catal. B* **2002**, *39*, 75–90. [[CrossRef](#)]
4. Yu, M.; Wang, J.; Tang, L.; Feng, C.; Liu, H.; Zhang, H.; Peng, B.; Chen, Z.; Xie, Q. Intimate coupling of photocatalysis and biodegradation for wastewater treatment: Mechanisms, recent advances and environmental applications. *Water Res.* **2020**, *175*, 115673. [[CrossRef](#)] [[PubMed](#)]
5. Obotey-Ezugbe, E.; Rathilal, S. Membrane technologies in wastewater treatment: A review. *Membranes* **2020**, *10*, 89. [[CrossRef](#)]
6. Belhouchat, N.; Zaghouane-Boudiaf, H.; Viseras, C. Removal of anionic and cationic dyes from aqueous solution with activated organo-bentonite/sodium alginate encapsulated beads. *Appl. Clay Sci.* **2017**, *135*, 9–15. [[CrossRef](#)]
7. Debnath, S.; Ballav, N.; Maity, A.; Pillay, K. Competitive adsorption of ternary dye mixture using pine cone powder modified with β -cyclodextrin. *J. Mol. Liq.* **2017**, *225*, 679–688. [[CrossRef](#)]
8. Liu, Y.; Zhu, L. Enhanced treatment of dispersed dye-production wastewater by self-assembled organobentonite in a one-step process with poly-aluminium chloride. *Sci. Rep.* **2017**, *7*, 6843. [[CrossRef](#)]
9. Yu, Y.; Wu, B.; Jiang, L.; Zhang, X.X.; Ren, H.Q.; Li, M. Comparative analysis of toxicity reduction of wastewater in twelve industrial park wastewater treatment plants based on battery of toxicity assays. *Sci. Rep.* **2019**, *9*, 3751. [[CrossRef](#)]
10. Ge, J.; Zhang, Y.; Heo, Y.J.; Park, S.J. Advanced design and synthesis of composite photocatalysts for the remediation of wastewater: A review. *Catalysts* **2019**, *9*, 122. [[CrossRef](#)]
11. Nethi, S.K.; Anand, N.A.; Rico-Oller, B.; Rodriguez-Dieguez, A.; Gomez-Ruiz, S.; Patra, C.R. Design, synthesis and characterization of doped-titanium oxide nanomaterials with environmental and angiogenic applications. *Sci. Total Environ.* **2017**, *599*, 1263–1274. [[CrossRef](#)] [[PubMed](#)]
12. Ku, Y.; Wang, L.C.; Ma, C.M.; Chou, Y.C. Photocatalytic oxidation of reactive red 22 in aqueous solution using $\text{La}_2\text{Ti}_2\text{O}_7$ photocatalyst. *Water Air Soil Pollut.* **2011**, *215*, 97–103. [[CrossRef](#)]
13. Ma, C.M.; Hong, G.B.; Chen, H.W.; Hang, N.T.; Shen, Y.S. Photooxidation contribution study on the decomposition of azo dyes in aqueous solutions by VUV-based AOPs. *Int. J. Photoenergy* **2011**, *2011*, 1–8. [[CrossRef](#)]
14. Zhao, C.; Zhou, Y.; de-Ridder, D.J.; Zhai, J.; Wei, Y.; Deng, H. Advantages of $\text{TiO}_2/5\text{A}$ composite catalyst for photocatalytic degradation of antibiotic oxytetracycline in aqueous solution: Comparison between TiO_2 and $\text{TiO}_2/5\text{A}$ composite system. *Chem. Eng. J.* **2014**, *248*, 280–289. [[CrossRef](#)]
15. Ochiai, T.; Nakata, K.; Murakami, T.; Fujishima, A.; Yao, Y.; Tryk, D.A.; Kubota, Y. Development of solar-driven electrochemical and photocatalytic water treatment system using a boron-doped diamond electrode and TiO_2 photocatalyst. *Water Res.* **2010**, *44*, 904–910. [[CrossRef](#)]
16. Ma, C.M.; Ku, Y.; Kuo, Y.L.; Chou, Y.C.; Jeng, F.T. Effects of silver on the photocatalytic degradation of gaseous isopropanol. *Water Air Soil Pollut.* **2009**, *197*, 313–321. [[CrossRef](#)]
17. Sayed, M.; Shah, L.A.; Khan, J.A.; Shah, N.S.; Nisar, J.; Khan, H.M.; Zhang, P.; Khan, A.R. Efficient photocatalytic degradation of norfloxacin in aqueous media by hydrothermally synthesized immobilized TiO_2/Ti films with exposed {001} facets. *J. Phys. Chem. A* **2016**, *120*, 9916–9931. [[CrossRef](#)]
18. Mohanta, D.; Ahmaruzzaman, M. Tin oxide nanostructured materials: An overview of recent developments in synthesis, modifications and potential applications. *RSC Adv.* **2016**, *6*, 110996–111015. [[CrossRef](#)]
19. Muneer, I.; Farrukh, M.A.; Shaghraf, S.; Khaleeq-Ur-Rahman, M.; Umar, A.A.; Adnan, R. Solvent controlled synthesis of tin oxide nanocatalysts and their applications in photodegradation of environmental hazardous materials. *Mater. Sci. Forum* **2013**, *756*, 197–204. [[CrossRef](#)]
20. Chen, S.; Sun, Z.; Zhang, L.; Xie, H. Photodegradation of gas phase benzene by SnO_2 nanoparticles by direct hole oxidation mechanism. *Catalysts* **2020**, *10*, 117. [[CrossRef](#)]

21. Shamaila, S.; Sajjad, A.K.L.; Ryma, N.U.A.; Farooqi, S.A.; Jabeen, N.; Majeed, S.; Farooq, I. Advancements in nanoparticle fabrication by hazard free eco-friendly green routes. *Appl. Mater. Today* **2016**, *5*, 150–199. [[CrossRef](#)]
22. Vatanparast, M.; Taghizadeh, M.T. One-Step hydrothermal synthesis of tin dioxide nanoparticles and its photocatalytic degradation of methylene blue. *J. Mater. Sci. Mater. Electron.* **2016**, *27*, 54–63. [[CrossRef](#)]
23. Mani, R.; Vivekanandan, K.; Subiramaniyam, N.P. Photocatalytic activity of different organic dyes by using pure and Fe doped SnO₂ nanopowders catalyst under UV light irradiation. *J. Mater. Sci. Mater. Electron.* **2017**, *28*, 13846–13852. [[CrossRef](#)]
24. Suligoj, A.; Pavlovic, J.; Arcon, I.; Rajic, N.; Novak Tucar, N. SnO₂-containing clinoptilolite as a composite photocatalyst for dyes removal from wastewater under solar light. *Catalysts* **2020**, *10*, 253. [[CrossRef](#)]
25. Han, K.; Peng, X.-L.; Li, F.; Yao, M.-M. SnO₂ composite films for enhanced photocatalytic activities. *Catalysts* **2018**, *8*, 453. [[CrossRef](#)]
26. Ali-Baig, A.B.; Rathinam, V.; Palaninathan, J. Fabrication of Zr-doped SnO₂ nanoparticles with synergistic influence for improved visible-light photocatalytic action and antibacterial performance. *Appl. Water Sci.* **2020**, *10*, 54. [[CrossRef](#)]
27. Al-Hamdi, A.M.; Sillanpaa, M.; Dutta, J. Photocatalytic degradation of phenol by iodine doped tin oxide nanoparticles under UV and sunlight irradiation. *J. Alloys Compd.* **2015**, *618*, 366–371. [[CrossRef](#)]
28. Li, P.G.; Lei, M.; Tanga, W.H.; Guoa, X.; Wang, X. Facile route to straight SnO₂ nanowires and their optical properties. *J. Alloys Compd.* **2009**, *477*, 515–518. [[CrossRef](#)]
29. Song, K.H.; Kang, Y. Preparation of high surface area tin oxide powders by a homogeneous precipitation method. *Mater. Lett.* **2000**, *42*, 283–289. [[CrossRef](#)]
30. Jana, S.; Mitra, B.C.; Bera, P.; Sikdar, M.; Mondal, A. Photocatalytic activity of galvanically synthesized nanostructure SnO₂ thin films. *J. Alloy. Compd.* **2014**, *602*, 42–48. [[CrossRef](#)]
31. Kim, S.P.; Choi, M.Y.; Choi, H.C. Photocatalytic activity of SnO₂ nanoparticles in methylene blue degradation. *Mater. Res. Bull.* **2016**, *74*, 85–89. [[CrossRef](#)]
32. Chakraborty, S.; Roy, M.; Saha, R. Cost-Effective synthesis method of facile environment friendly SnO₂ nanoparticle for efficient photocatalytic degradation of water contaminating compound. *Water Sci. Technol.* **2020**, *8*, 508–517. [[CrossRef](#)]
33. Li, L.; Ma, Q.; Wang, S.; Song, S.; Li, B.; Guo, R.; Cheng, X.; Cheng, Q. Photocatalytic performance and degradation mechanism of aspirin by TiO₂ through response surface methodology. *Catalysts* **2018**, *8*, 118. [[CrossRef](#)]
34. Ma, C.M.; Cheng, C.L.; Lee, S.C.; Hong, G.B. Antioxidant capacity, insecticidal ability and heat-oxidation stability of tagetes lemmonii leaf extract. *Ecotoxicol. Environ. Saf.* **2018**, *151*, 68–75. [[CrossRef](#)] [[PubMed](#)]
35. Hong, G.B.; Wang, Y.K. Synthesis of low-cost adsorbent from rice bran for the removal of reactive dye based on the response surface methodology. *Appl. Surf. Sci.* **2017**, *423*, 800–809. [[CrossRef](#)]
36. Nair, A.T.; Makwana, A.R.; Ahammed, M.M. The use of response surface methodology for modelling and analysis of water and wastewater treatment processes: A review. *Water Sci. Technol.* **2014**, *69*, 464–478. [[CrossRef](#)]
37. Akkaya, G.K.; Erkan, H.S.; Sekman, E.; Top, S.; Karaman, H.; Bilgili, M.S.; Engin, G.O. Modeling and optimizing Fenton and electro-Fenton processes for dairy wastewater treatment using response surface methodology. *Int. J. Environ. Sci. Technol.* **2019**, *16*, 2343–2358. [[CrossRef](#)]
38. Al-Hamdi, A.M.; Rinner, U.; Sillanpaa, M. Tin dioxide as a photocatalyst for water treatment: A review. *Process. Saf. Environ. Prot.* **2017**, *107*, 190–205. [[CrossRef](#)]
39. Upadhaya, D.; Talinungsang; Kumar, P.; Purkayastha, D.P. Tuning the wettability and photocatalytic efficiency of heterostructure ZnO-SnO₂ composite films with annealing temperature. *Mater. Sci. Semicond. Process.* **2019**, *95*, 28–34. [[CrossRef](#)]
40. Al-Hamdi, A.M.; Sillanpaa, M.; Dutta, J. Intermediate formation during photodegradation of phenol using lanthanum doped tin dioxide nanoparticles. *Res. Chem. Intermed.* **2016**, *42*, 3055–3069. [[CrossRef](#)]
41. Cui, Y.H.; Feng, Y.J.; Liu, J.; Ren, N. Comparison of various organic compounds destruction on rare earths doped Ti/Sb-SnO₂ electrodes. *J. Hazard. Mater.* **2012**, *239*, 225–232. [[CrossRef](#)] [[PubMed](#)]
42. Ghosh, S.; Roy, S. Effect of ageing on Sn₆O₄(OH)₄ in aqueous medium—simultaneous production of SnO and SnO₂ nanoparticles at room temperature. *J. Solgel. Sci. Technol.* **2016**, *81*, 769–773. [[CrossRef](#)]

43. Ibarguen, C.A.; Mosquera, A.; Parra, R.; Castro, M.S.; Rodriguez-Paez, J.E. Synthesis of SnO₂ nanoparticles through the controlled precipitation route. *Mater. Chem. Phys.* **2007**, *101*, 433–440. [[CrossRef](#)]
44. Moreno, M.S.; Punte, G.; Rigotti, G.; Mercader, R.C.; Weisz, A.D.; Blesa, M.A. Kinetic study of the disproportionation of tin monoxide. *Solid State Ion.* **2001**, *144*, 81–86. [[CrossRef](#)]
45. Sinha, A.K.; Pradhan, M.; Sarkar, S.; Pal, T. Large-Scale solid-state synthesis of Sn–SnO₂ nanoparticles from layered SnO by sunlight: A material for dye degradation in water by photocatalytic reaction. *Environ. Sci. Technol.* **2013**, *47*, 2339–2345. [[CrossRef](#)] [[PubMed](#)]
46. Bhattacharjee, A.; Ahmaruzzaman, M.; Devi, T.B.; Nath, J. Photodegradation of methyl violet 6B and methylene blue using tin-oxide nanoparticles (synthesized via a green route). *J. Photochem. Photobiol. A* **2016**, *325*, 116–124. [[CrossRef](#)]
47. Ilka, M.; Bera, S.; Kwon, S.H. Influence of Surface Defects and Size on Photochemical Properties of SnO₂ Nanoparticles. *Materials* **2018**, *11*, 904. [[CrossRef](#)]
48. Nejati, K. Synthesis by precipitation method and investigation of SnO₂ nanoparticles. *Cryst. Res. Technol.* **2012**, *47*, 567–572. [[CrossRef](#)]
49. Santos, S.C.R.; Oliveira, A.F.M.; Boaventura, R.A.R. Bentonitic clay as adsorbent for the decolourisation of dyehouse effluents. *J. Clean. Prod.* **2016**, *126*, 667–676. [[CrossRef](#)]
50. O'Donnell, K.P.; Chen, X. Temperature dependence of semiconductor band gaps. *Appl. Phys. Lett.* **1991**, *58*, 2924–2926. [[CrossRef](#)]
51. Rai, R.C.; Guminiak, M.; Wilser, S.; Cai, B.; Nakarmi, M.L. Elevated temperature dependence of energy band gap of ZnO thin films grown by e-beam deposition. *J. Appl. Phys.* **2012**, *111*, 073511. [[CrossRef](#)]
52. Zhu, Z.; Zhang, A.; Ouyang, G.; Yang, G. Band gap tunability in semiconductor nanocrystals by strain: Size and temperature effect. *J. Phys. Chem. C* **2011**, *115*, 6462–6466. [[CrossRef](#)]
53. Mourabet, M.; Rhilassi, A.E.; Boujaady, H.E.; Bennani-Ziatni, M.; Hamri, R.E.; Taitai, A. Removal of fluoride from aqueous solution by adsorption on hydroxyapatite (HAp) using response surface methodology. *J. Saudi Chem. Soc.* **2015**, *19*, 603–615. [[CrossRef](#)]
54. Fakhri, A. Application of response surface methodology to optimize the process variables for fluoride ion removal using maghemite nanoparticles. *J. Saudi Chem. Soc.* **2014**, *18*, 340–347. [[CrossRef](#)]
55. Cao, R.; Fan, M.; Hu, J.; Ruan, W.; Xiong, K.; Wei, X. Optimizing low-concentration mercury removal from aqueous solutions by reduced graphene oxide-supported Fe₃O₄ composites with the aid of an artificial neural network and genetic algorithm. *Materials* **2017**, *10*, 1279. [[CrossRef](#)]
56. Pham, V.T.; TNguyen, H.-T.; Thi Cam Nguyen, D.; TN Le, H.; Thi Nguyen, T.; Thi Hong Le, N.; Lim, K.T.; Duy Nguyen, T.; Tran, T.V.; Bach, L.G. Process optimization by a response surface methodology for adsorption of congo red dye onto exfoliated graphite-decorated MnFe₂O₄ nanocomposite: The pivotal role of surface chemistry. *Processes* **2019**, *7*, 305. [[CrossRef](#)]
57. Sadeghzadeh-Attar, A. Efficient photocatalytic degradation of methylene blue dye by SnO₂ nanotubes synthesized at different calcination temperatures. *Sol. Energy Mater. Sol. Cells* **2018**, *183*, 16–27. [[CrossRef](#)]
58. Viet, P.V.; Thi, C.M.; Hieu, L.V. The high photocatalytic activity of SnO₂ nanoparticles synthesized by hydrothermal method. *J. Nanomater.* **2016**, *2016*, 1–8.
59. Nasir, Z.; Shakir, M.; Wahab, R.; Shoeb, M.; Alam, P.; Khan, R.H.; Mobin, M.; Lutfullah. Co-Precipitation synthesis and characterization of Co doped SnO₂ NPs, HSA interaction via various spectroscopic techniques and their antimicrobial and photocatalytic activities. *Int. J. Biol. Macromol.* **2017**, *94*, 554–565. [[CrossRef](#)]
60. Osuntokun, J.; Onwudiwe, D.C.; Ebenso, E.E. Biosynthesis and photocatalytic properties of SnO₂ nanoparticles prepared using aqueous extract of cauliflower. *J. Clust. Sci.* **2017**, *28*, 1883–1896. [[CrossRef](#)]
61. Nuray Guy, N.; Çakar, S.; Ozacar, M. Comparison of palladium/zinc oxide photocatalysts prepared by different palladium doping methods for congo red degradation. *J. Colloid Interface Sci.* **2016**, *466*, 128–137.
62. Rupa, E.J.; Kaliraj, L.; Abid, S.; Yang, D.C.; Jung, S.K. Synthesis of a zinc oxide nanoflower photocatalyst from sea buckthorn fruit for degradation of industrial dyes in wastewater treatment. *Nanomaterials* **2019**, *9*, 1692. [[CrossRef](#)] [[PubMed](#)]

